Dalton Transactions

ROYAL SOCIETY OF CHEMISTRY

PAPER

View Article Online
View Journal | View Issue

Check for updates

Cite this: *Dalton Trans.*, 2025, **54**, 6538

Exploring pseudohalide substitution in α-cobalt-based layered hydroxides†

Youssra Diouane, ‡ Alvaro Seijas-Da Silva, ‡ Víctor Oestreicher § and Gonzalo Abellán *

Received 3rd February 2025,
Accepted 11th March 2025

DOI: 10.1039/d5dt00273g

rsc.li/dalton

While halide substitution has significantly influenced the electrical and magnetic properties of α-layered hydroxide frameworks (α-LH), the incorporation of pseudohalides remains limited. In this study, we present a detailed investigation of two-dimensional cobalt-layered hydroxides modified with tricyanomethanide ($C_4N_3^-$) and thiocyanate (SCN^-) pseudohalides, synthesized *via* a simple epoxide route at room temperature. Pseudohalide incorporation induces subtle structural modifications relative to pristine cobalt-chloride layered hydroxide (α-Co-Cl), including changes in interlayer spacing and the confirmation of a distinct bridging coordination in thiocyanate-modified samples. Magnetic measurements reveal broadly similar behavior across all samples, with the thiocyanate compound reflecting a structural difference that affects its magnetic response. These findings underscore the influence of pseudohalides on the structure and the effect of pseudohalide substitution on the magnetic response of α-cobalt-based layered hydroxides, demonstrating the chemical and structural versatility of *Simonkolleite*-like hydroxides as tunable materials for designing novel hybrids with dynamic structures.

Introduction

Two-dimensional transition metal-based layered hydroxides (LH) are a class of clay materials characterized by their lamellar structure and wide chemical and structural versatility, making them appealing in different domains.[1–3] This wide structural versatility can be exemplified by three main crystallographic phases. The first one is the Brucite-like structure[4] (β-structure) where the metal is arranged at the octahedral position and the interlayer space is defined by van der Waals interaction. This structure is characterized by its stacked layers. The second one is the hydrotalcite-like structure, also called layered double hydroxide (LDH), which is recognized by the formula $M^{II}_{1-x}M^{III}_{x}(OH)_2A^{n-}_{x/n}{\cdot}m(H_2O)$. The LDH comprises divalent and trivalent metals in the same layer and both are arranged at the octahedral position.[5] The last one is the *Simonkolleite*-like structure[6] (α-structure or α-LH) with the formula $M^{Oh}_{1-x}M^{Td}_{x}(OH)_{2-x}A^{n-}_{x/n}{\cdot}m(H_2O)$, containing only divalent metals arranged at the tetrahedral (Td) and octahedral (Oh) positions.[7] For instance, in the α-structure, the interlayer spacing can be adjusted by altering the inserted anion. Importantly, since this structure contains tetrahedral metal centers, the anions are covalently bonded to the metal, allowing for modulation of the electronic properties.[8–10] Overall, these materials are commonly known for their tunable properties which make them attractive in various fields, such as energy systems and magnetism.[11–13]

This type of framework is characterized by short distances between metal atoms, facilitated by the μ_3 coordination mode of the OH– groups in the hydroxide layers, which leads to a sprawling metal lattice. This arrangement promotes magnetic interactions *via* superexchange coupling along metal–oxygen–metal pathways, resulting in a diverse range of 2D magnetic behaviors, including ferromagnetism, antiferromagnetism, and ferrimagnetism. Furthermore, modifying the layer's functionality affects the structure and is directly reflected in the modulations of the properties of these layered transition metal hydroxides.[14,15] In our previous works focused on nickel-based layered hydroxides, a ferrimagnetic behavior is observed where the addition of the antiferromagnetic M^{2+}–OH–M^{3+} and M^{3+}–OH–M^{3+} coupled pairs to the ferromagnetic M^{2+}–OH–M^{2+} pairs takes place. In contrast, cobalt-based layered hydroxides, whether in LDH or α structure, display a predominant ferromagnetic behavior. Specifically, ferromagnetic (FM) interactions are expected between Co ions in identical coordination environments (Oh–Oh and Td–Td), while antiferromagnetic (AFM) interactions are anticipated between Co ions in different environments (Oh–Td).[6,16–18]

Halides are families that have been most studied to modify *Simonkolleite*-like structures. However, despite their similar

Instituto de Ciencia Molecular (ICMol), Universidad de Valencia, Catedrático José Beltrán Martínez, 2, 46980 Paterna, Valencia, Spain. E-mail: gonzalo.abellan@uv.es

†Electronic supplementary information (ESI) available. See DOI: https://doi.org/10.1039/d5dt00273g

‡These authors contributed equally to this work.

§Current Address: TECNALIA Research and Development, Mikeletegi Pasealekua 2, 20009, San Sebastian-Donostia, Spain.

properties, only the incorporation of tricyanomethanide into the layered hydroxide structure has been achieved among pseudohalides.[19] On the one hand, pseudohalides exhibit chemical properties and behavior that closely resemble those of true halide ions such as chloride. Despite containing multiple internal bonds, which might be expected to influence their reactivity, their chemical behavior remains unaffected.[20–22] This suggests that these internal multiple bonds do not significantly determine their overall chemical characteristics. On the other hand, pseudohalide substitution has been explored in different classes of materials, demonstrating its effect on their performance in several fields such as energy and magnetism.[19,23–26] The most common pseudohalides are tricyanomethanide (C_4N_3–) and thiocyanate (SCN–). Moreover, pseudohalides are known to exhibit a wide range of electrochemical behaviors, such as cyanide (CN–), which can act as a reducing agent, while thiocyanate (SCN–) can act as both an oxidizing and reducing agent.

Herein, we will lay out a straightforward and reproducible synthetic route allowing the modulation of the anion's nature and arrangement in the interlayer space. This work aims to explore the structural, morphological and magnetic responses of layered hydroxides incorporating thiocyanate and tricyanomethanide in a Co-based α-structure (Scheme 1). Thiocyanate, known for its resonance structure, exhibits bridging between the layers of α-LH, highlighting the possibility of modulating the structure of the layered hydroxide material. Regarding the magnetic response, these phases behave similarly to previously literature reported α-Co hydroxides, exhibiting magnetic ordering below 50 K. All exhibit a positive Curie–Weiss temperature due to the predominance of ferromagnetic ordering. Upon examining the temperature at which magnetic ordering occurs (T_B, T_M), a slight difference is observed in pseudohalide-substituted compounds. All exhibit characteristics of hard magnets with a coercive field higher than 1000 Oe.

This work opens the way for developing novel materials incorporating less-explored pseudohalide ligands, with a particular focus on their structural effects. Notably, the thiocyanate compound exhibits a time-dependent structural evolution, highlighting the role of pseudohalides in material architecture. This structural transformation aligns with the observed magnetic response, where subtle changes reflect the influence of interlayer modifications on magnetic behavior.

Experimental methods

Materials and reagents

NaCl (Aldrich, 99%), NaSCN (Aldrich, 99.99%), NaC_4N_3 (Tokyo Chemical Industry, 98%), glycidol (Aldrich, 96%), and $CoCl_2{\cdot}6H_2O$ (Tokyo Chemical Industry, 98%). 250 mM $CoCl_2{\cdot}6H_2O$ was prepared in deionized water, and pH = 3 water (adjusted with HCl) was used for all the syntheses below to guarantee the precipitation of all species.

Synthesis of layered hydroxides

In this work, α-Co-Cl is used to compare the thiocyanate materials with the halide compounds. The sample was prepared following the same protocol, mixing 100 mM NaCl, 1000 mM glycidol, and 10 mM $CoCl_2$ in a 1 : 1 v/v ratio of H_2O : EtOH.[6,8,27,28] The solution was filtered after 24 hours of precipitation. The green precipitate was washed several times with Milli-Q water and ethanol and then dried overnight in a desiccator with dry silica.

The synthesis of thiocyanate substituted α-Co-SCN was carried out using the epoxide route by adding 100 mM NaSCN, different concentrations of glycidol (500 mM and 1000 mM), and 10 mM $CoCl_2$ in a 1 : 1 v/v ratio of H_2O : EtOH. The precipitate was collected by filtering the solution within 24 hours. The solid was washed several times with Milli-Q water and ethanol and then dried overnight in a desiccator with dry silica.

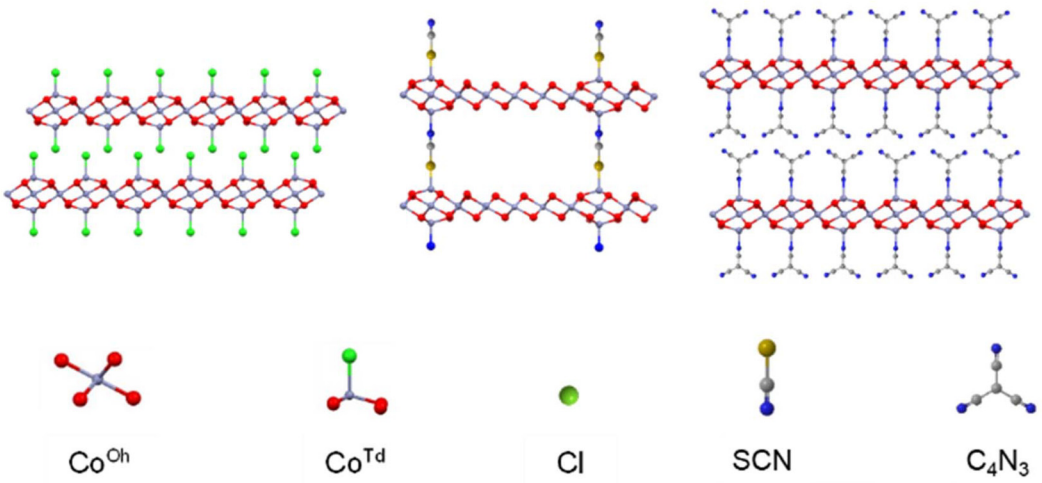

Scheme 1 Representation of α-Co-Cl, α-Co-SCN, and α-Co-C_4N_3. The axial ligands of octahedral cobalt are not observed with this crystal orientation.

α-Co-C_4N_3 was obtained by blending 100 mM NaC_4N_3, 1000 mM glycidol and 10 mM $CoCl_2$ in a 3 : 1 v/v ratio of H_2O : EtOH. 50 mM of the nucleophile NaCl was added to promote the precipitation. After 48 hours, the precipitate was washed multiple times with Milli-Q water and ethanol before letting the solid dry in a desiccator with dry silica overnight.

Chemical and structural characterization

Powder X-ray diffraction (PXRD) patterns were obtained employing a PANalytical Empyrean X-ray diffractometer with a capillary platform and copper radiation (Cu Kα = 1.54178 Å) in the 2-theta range of 2–70°. UV/Vis absorption spectra of the solid samples were recorded in reflectance mode employing a Jasco V-670 spectrometer. The attenuated total reflectance Fourier-transform infrared (ATR-FTIR) spectra were collected with an Agilent Cary 630 FTIR spectrometer in the 4000–650 cm^{-1} range in the absence of KBr pellets. Field emission scanning electron microscopy (FESEM) and energy dispersive X-ray spectroscopy (EDS) studies were performed on a Hitachi S-4800 microscope at an accelerating voltage of 20 kV. X-ray photoelectron spectroscopy (XPS) spectra were recorded using a Thermo Scientific™ K-Alpha X-ray Photoelectron Spectrometer. XPS data were analysed using Advantage software. Thermogravimetric analysis (TGA) of all samples was performed on a Mettler Toledo TGA/DSC2 apparatus in the 25–700 °C temperature range at a 10 °C min^{-1} scan rate and synthetic air flow of 100 mL min^{-1} (80% N_2 + 20% O_2) or pure N_2. Carbon, nitrogen, hydrogen, and sulphur contents were determined by microanalytical procedures by using an LECO CHNS-932. The pH meter HANNA HI5221 is equipped with an automatic temperature compensation (ATC) feature that adjusts pH readings to account for temperature changes, ensuring more accurate results. It supports a temperature range of −20.0 °C to 120.0 °C.

Magnetic characterization

Magnetic data were collected on the bulk materials with a Quantum Design superconducting quantum interference device (SQUID) MPMS-XL-5. The magnetic susceptibility of the samples was corrected by considering the diamagnetic contributions of their atomic constituents as deduced from Pascal's constant tables, the sample holder, and *n*-eicosane. The DC data were obtained with a SQUID in a plastic holder under an external applied field of 100 or 1000 Oe in the 2–300 K temperature range. Magnetization studies were performed with a SQUID, between −5 and +5 T at a constant temperature of 2 K. To prepare the sample for magnetization measurement, a mixture of the sample and *n*-eicosane was prepared. *n*-Eicosane is a non-polar and non-magnetic substance. In this case, it was used as a passive matrix or encapsulation material to avoid the preferred alignment of the crystallites. By surrounding the magnetic particles, *n*-eicosane reduces dipole–dipole interactions between them and provides a homogeneous and stable environment.[29] The AC data were collected with a Quantum Design physical property measurement system PPMS9, under an applied field of 3.96 Oe at 1 Hz.

Results and discussion

Synthesis and structural characterization

The epoxide route is adopted as it provides an optimal synthetic mild environment for achieving the desired α-phase, using the reaction of α-Co-Cl as a reference.[8,30] In this work, we aim to achieve a covalent bond between the tetrahedral cobalt and the ligands, namely, thiocyanate (SCN) and tricyanomethanide (C_4N_3). For this purpose, the first study explores the ability of the two ligands to open the ring of the epoxide, as this mechanism facilitates the generation of hydroxides and increases the pH to finally create the appropriate environment for the metal to precipitate. The pH meter we use, although typically used for aqueous media, is employed here to monitor the reaction progress by identifying the starting point and the end of the precipitation process in a 1 : 1 (v/v) ratio of H_2O : EtOH mixture. While the exact pH value is not critical in this context, it remains close to the known precipitation pH of cobalt in water, as illustrated in Fig. S1.† The amounts of NaX (X = Cl, SCN, C_4N_3) and glycidol, corresponding to the concentrations of 100 mM and 1000 mM, respectively, were weighed and used for this synthesis without any metal as shown in Fig. 1a. We can observe that the pH of thiocyanate increases within a couple of minutes and faster than that of the chloride compound which makes it a better nucleophile in this process. However, the pH remains equal to 3 for the sample containing tricyanomethanide. This result shows that tricyanomethanide needs a nucleophilic compound such as NaCl to help carry out the synthesis.

The same amounts of epoxide (glycidol, 1000 mM) and $CoCl_2$ (10 mM) were incorporated to ensure the purity of each sample. The equivalent amount of 100 mM NaX (X = Cl, SCN, C_4N_3) was added to the mixtures. The solvent used is a mixture of water and ethanol where the pH of Milli-Q water is adjusted to 3 to have approximately the same starting pH. Ethanol is used to ensure a flower-like morphology and avoid magnetic behaviour modifications related to the morphology.[27,31] The metal cobalt II precipitates around pH ∼ 7–8. The precipitation plateau is expected around that pH value. The compound α-Co-Cl starts with pH ∼ 3 and the alkalinization takes place immediately; an overshoot is observed after 20 min at pH = 7.7 (Fig. 1b). The precipitation plateau is reached at pH = 7.8 readjusting to pH = 8.8 with the release of hydroxide from the epoxide until the end of the plateau within 18 h of reaction. For the synthesis of α-Co-SCN, the reaction begins with the same pH ∼ 3 but the reaction is much faster. The precipitation plateau starts within 1 min at pH = 8.1. The precipitation ends within 23 min. The reaction of the chloride sample takes more time than that of thiocyanate to end. Both α-Co-Cl and α-Co-SCN solids are collected after 24 hours of precipitation. For α-Co-C_4N_3, the concentration of the salt in the above syntheses was maintained ([NaC_4N_3] = 100 mM); however, 50 mM NaCl was added to guarantee proper alkalinization as demonstrated in Fig. 1a. The pH curve of α-Co-C_4N_3 exhibits a rise for 2.2 h until reaching the plateau at pH = 7.8. The metal precipitation took almost 48 hours. The solution was filtered after 48 hours of precipitation.

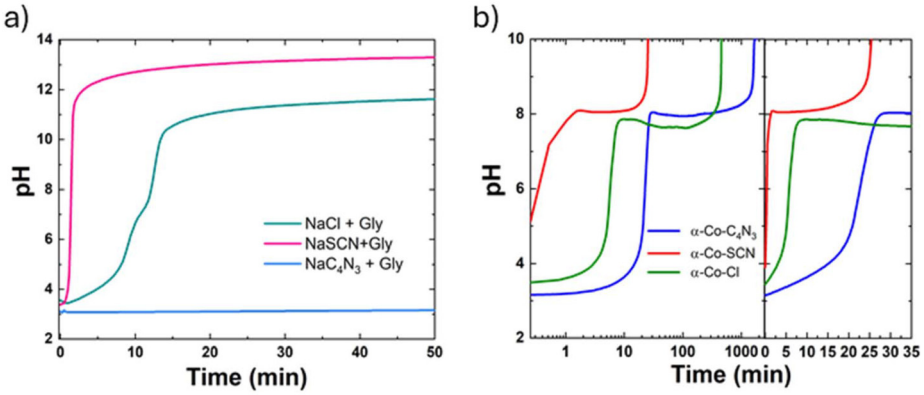

Fig. 1 (a) pH measurements of the pre-synthesis using the precursors: NaCl, NaSCN, and NaC_4N_3 with 1000 mM glycidol and without any metal. (b) Precipitation curves of the different compounds synthesized: α-Co-Cl, α-Co-SCN, and α-Co-C_4N_3. This experiment was carried out at room temperature, under magnetic stirring. The measurement starts after pH value stabilization and the addition of glycidol to the mixture.

To achieve the desired phase containing tricyanomethanide, we used a higher concentration of glycidol than previously reported,[8] as the usual range was ineffective. We maintained the same amount of epoxide across all three syntheses. Furthermore, a precise concentration of NaCl (50 mM) was added to α-Co-C_4N_3 to ensure alkalinization and avoid incorporating chloride into the structure as shown in Fig. S2.† Upon increasing the NaCl concentration to 100 mM, chloride easily integrates into the structure. Fig. S2† shows similarities between the X-ray diffraction peaks of α-Co-Cl and α-Co-C_4N_3 treated with 100 mM NaCl.

Several characterization techniques such as X-ray powder diffraction (XRPD), UV-Vis, and attenuated total reflectance Fourier-transform infrared spectroscopy (ATR-FTIR), shown in Fig. 2, have been used to identify the structure of the materials and collect details about the nature of the interlayer anion and the basal space distance.

Fig. 2a displays the similarity between the *Simonkolleite* phase and our materials.[8,32] The XRPD patterns of α-Co-Cl and α-Co-C_4N_3 exhibit sharp and well-defined peaks compared to the α-Co-SCN compound, indicative of a higher crystallite size.[33] However, the first peak corresponding to the (003) plane between 5° and 10° remains visible in all three samples, allowing us to determine the basal distance. The shift of this peak also suggests a change in the interlayer spacing.[34] Moreover, none of the samples present magnetic impurities such as spinel traces.[35] With the latter's position, we calculate the basal distance with Bragg's law: $n\lambda = 2d \sin\theta$. α-Co-Cl exhibits an interlayer distance of 8.07 Å in agreement with the previous literature.[8] The basal distance of α-Co-SCN and α-Co-C_4N_3 is equal to 9.16 and 11.46 Å respectively, in line with the bigger molecular size.[36] Moreover, the intralayer distance extracted from the (110) plane situated around $2\theta \sim 58.7°$ is not altered by halide/pseudohalide substitution (a = 3.13 ± 0.01 Å in all three compounds).[6,8]

Attenuated total reflectance Fourier-transform infrared spectroscopy (ATR-FTIR) as well as UV-Vis gives us information

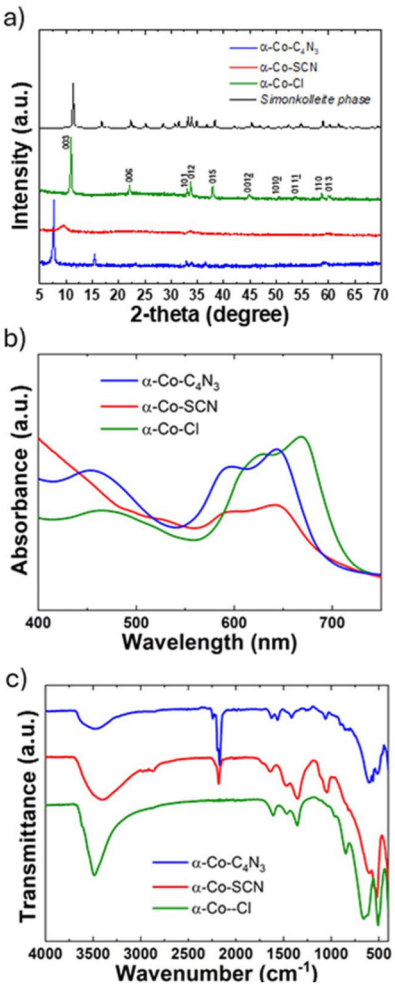

Fig. 2 (a) X-ray powder diffraction, (b) UV-Vis and (c) attenuated total reflectance Fourier-transform infrared spectroscopy (ATR-FTIR) of α-Co-Cl, α-Co-SCN, and α-Co-C_4N_3.

about the elements and the interlayer anions in the structure. Fig. 2b presents the UV-Vis diffuse reflectance spectrum, which displays absorbance as a function of wavelength. The absorbance values are arbitrary due to variations in the amount of powder used for each sample. The spectrum shows a double peak between 600 and 700 cm^{-1} and a single peak at a lower wavelength. The double peak confirms the existence of cobalt at the tetrahedral position.[37] Also, its shifting is related to the cobalt environment.[6,8,36] Fig. 2b exhibits a double peak at ~668.5, ~643.5 and ~641 nm for α-Co-Cl, α-Co-C_4N_3, and α-Co-SCN respectively, indicative of cobalt at the tetrahedral positions, suggesting a specific arrangement of cobalt ions within the material's layers, consistent with the *Simonkolleite*-like layered hydroxide structure. The peak at a lower wavelength around 480 cm^{-1} exhibits the presence of octahedral cobalt. The ATR-FTIR spectra in Fig. 2c show in all samples the peak of O–H at 3460, 3400, and 3492 cm^{-1} for α-Co-C_4N_3, α-Co-SCN and α-Co-Cl respectively. In addition, the peaks at lower wavelengths between 400 and 800 cm^{-1} exhibit metallic bands which refer to vibrational modes associated with the bonds between the metal and non-metal atoms.[31] Since the metal used in this case is cobalt, these peaks represent the vibrational bands of Co–O, Co–O–Co, and O–Co–O. Furthermore, the peak at 1624 cm^{-1} represents water in the structure exhibiting O–H bending. The presence of ethanol is manifested by several peaks as shown in Fig. S3.† The peaks at 1044 and 1473 cm^{-1} represent C–O stretching and antisymmetric bending of the C–H bond, respectively.[38] Also, C–H bending is observed at 879 cm^{-1}. Fig. 2c shows a sharp peak at 2070 cm^{-1} in the α-Co-C_4N_3 compound, indicating the presence of cyanate.[39] For α-Co-SCN, a peak beyond 2000 cm^{-1} is expected. Thiocyanate is known for its resonance structure whereas three bonding possibilities exist. SCN can show either a nitrogen or sulfur terminal or a bridging behavior. In a cobalt system, thiocyanate is usually bonded by nitrogen showing a peak around 2060 cm^{-1}, or by both sulfur and nitrogen exhibiting a peak above 2100 cm^{-1}, which makes the thiocyanate act like a bridge between the cobalt layers.[40–42] In this case, a peak at 2180 cm^{-1} is observed. Hence, α-Co-SCN shows a bridging behavior. These results confirm the presence of different anions in the interlayer space. Fig. 3 exhibits the TGA measurement of the materials through the temperature range, where the first mass drop is due to water loss. The degradation of α-Co-Cl through the same temperature range has been reported.[8] However, the thermogravimetric analysis of α-Co-C_4N_3 and α-Co-SCN shows drastic degradation at 244 °C and 240 °C, respectively, under a nitrogen atmosphere, recording a loss of Δm = 24.5% and Δm = 17.4%, respectively. A loss of Δm = 24.6% is observed in air at 235 °C for α-Co-C_4N_3 and Δm = 20% at 245 °C for α-Co-SCN, indicating the degradation of the material. The mass of α-Co-SCN increases slightly at 300 °C in air which can be explained by the formation of an eventual complex due to the presence of oxygen in the environment. This phenomenon is not observed under a nitrogen atmosphere.

In our previous works, TG-MS and TG-GC-MS have been performed on LH materials. These studies showed different

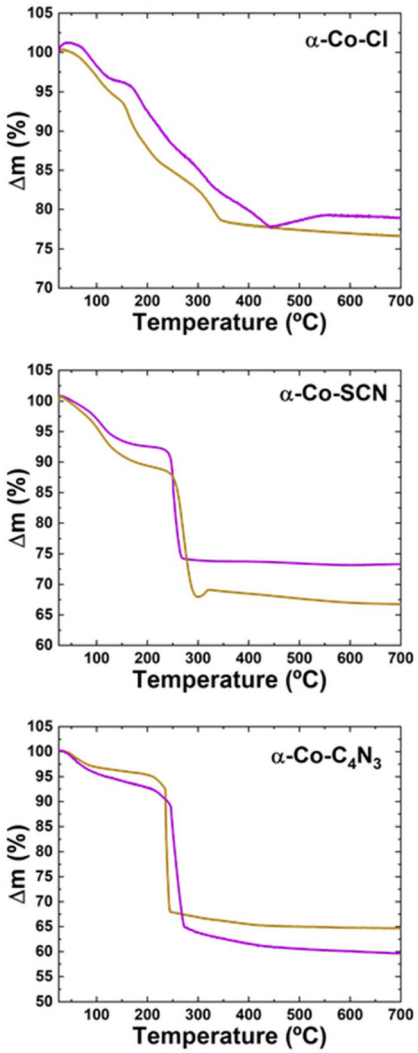

Fig. 3 TGA measurement of the samples α-Co-Cl, α-Co-SCN, and α-Co-C_4N_3 (brown) in air and (purple) in nitrogen (N_2).

steps of degradation between 25 °C and above 600 °C. The region between 200 and 600 °C corresponds to the dehydroxylation of the layered system, involving the elimination of chemisorbed water and the interlayer anion.[43–45] In this case, the pseudohalide compounds show different behavior than halide substitution. This drastic degradation prevents the identification of distinct degradation stages, indicating that this technique is not the most appropriate for quantifying the pseudohalide present in the structure.

The morphology has been explored by scanning electron microscopy (SEM) characterization. We observe that all samples in Fig. 4 have a flower-like morphology. The arrangement of the 2D hexagonal particles into the flower-like layered hydroxides is due to the velocity of the precipitation and the presence of ethanol.[27,46] This figure shows that α-Co-SCN exhibits thinner and less stiff petals compared to α-Co-Cl and α-Co-C_4N_3.

Furthermore, XPS characterization was performed. The corresponding XPS survey spectra in Fig. S4† further support

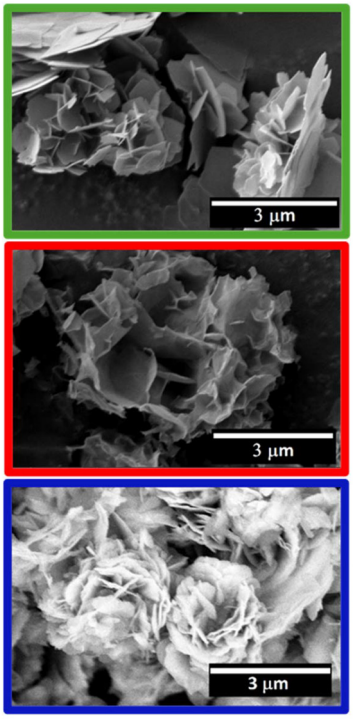

Fig. 4 Scanning electron microscopy images of (green) α-Co-Cl, (red) α-Co-SCN and (blue) α-Co-C_4N_3.

the elemental composition of each sample. The survey spectra in Fig. S4.1 and Fig. S4.2† clearly exhibit peaks corresponding to Co, Cl, C, and N, indicating the presence of chloride and tricyanomethanide ligands in the structure of α-Co-Cl and α-Co-C_4N_3, respectively.[47] In α-Co-SCN (Fig. S4.3†), the expected peaks for S and N are not clearly visible in the survey spectra. In this sense, high-resolution XPS of S and N confirms the presence of the SCN ligand in the sample (Fig. S5†). The estimated atomic ratio of Co : SCN is 12 : 1. This suggests a possible loss or substantial reduction in the incorporation of thiocyanate ligands, potentially due to ligand dissociation, degradation, or limited surface sensitivity in the XPS measurement. In addition, high-resolution XPS of Co (Fig. S6†) confirms the presence of cobalt in oxidation state II as evidenced by the characteristic Co 2p peaks. Specifically, the spectra exhibit well-defined Co $2p_{3/2}$ (~780.9 eV) and Co $2p_{1/2}$ (~780.9 eV) peaks with satellite features indicative of Co^{2+}.[48]

Elemental analysis was performed to define the quantity of the pseudohalide inserted into the interlayer space. The approximation was established with the percentage of the elements in the samples (summarized in Table 1). As a confirmation of the analysis above, all the samples contain the expected elements. However, in α-Co-SCN, the amount of SCN, as also shown in the XPS survey (Fig. S4.3†), is not comparable to the others; in fact, it is deficient, showing a low covalent modification in this sample. As a result, we have opted to improve the synthesis to adjust the substituent level, bringing it in line with the other two samples. Our main goal with this optimization is to ensure that all three samples have a comparable amount of the desired substituent, allowing a proper magnetic comparison of these three α phases, enabling more precise comparisons and insightful analysis between Cl, SCN, and C_4N_3 substitution (*vide infra*). Additionally, through this optimization, we aim to gain insights into the evolution of the sample, enhancing our understanding of its dynamic behavior and characteristics.

The same synthesis has been repeated with a lesser amount of glycidol (500 mM) to decrease the reaction rate and allow for a proper study of its evolution. In the same solution of 1 L total volume, we collect a solid from ~140 mL after 1 h, 2 h, 3 h, 4 h, 5 h, 6 h, and 24 h of precipitation (Fig. 5). The precipitation plateau starts within four minutes at pH = 8.1, similar to the previous thiocyanate sample. However, in this case, the precipitation ends within nearly 1 h, which is two times more than the previous synthesis. This was expected regarding the lower amount of epoxide used for this new compound. This strategy also allows us to slow down the precipitation process to gain a better insight into the material's evolution through time. The solids collected are α-Co-SCN-1 h, α-Co-SCN-2 h, α-Co-SCN-3 h, α-Co-SCN-4 h, α-Co-SCN-5 h, α-Co-SCN-6 h, and α-Co-SCN-24 hct.

Interestingly, the color of these compounds is not the same; α-Co-SCN-1 h is bluish-green and as the precipitation time increases, the solid becomes greener (Fig. S7†).

Although the crystallinity of the thiocyanate compounds remains weak, the XRPD in Fig. 6a shows the peak corresponding to the (003) plane. Thiocyanate evolution in the LH structure shows two different interlayer distances over time, exhibiting two structures. α-Co-SCN-1 h and α-Co-SCN-3 h exhibit one defined peak at $2\theta \sim 6.58°$ and 9.65° recording basal distances of 13.43 Å and 9.16 Å, respectively. The evolution of the thiocyanate reaction over time shows that the basal distance reduces from d_{BS} = 13.43 Å to 9.16 Å within 24 h. UV-Vis (Fig. 6b) indicates the double peak of tetrahedral cobalt that shifts from ~668.5 to ~641 nm from α-Co-Cl to α-Co-SCN respectively. The same shift of the previous synthesis is observed, which is once again due to the nature of the direct anion covalently attached to the cobalt at the

Table 1 The estimated formulas of the samples α-Co-Cl, α-Co-SCN, and α-Co-C_4N_3 established by elemental analysis

Sample	C%	N%	S%	H%	O%	Phase
α-Co-Cl	0.73	0	0	2.16	33.86	$Co^{Oh}_{0.81}Co^{Td}_{0.19}(OH)_{1.81}Cl_{0.19}(H_2O)_{0.1}(C_2H_6O)_{0.03}$
α-Co-C_4N_3	12.68	7.65	0	2.04	26.2	$Co^{Oh}_{0.78}Co^{Td}_{0.22}(OH)_{1.78}(C_4N_3)_{0.22}(H_2O)_{0.01}(C_2H_6O)_{0.18}$
α-Co-SCN	7.36	0.35	0.64	2.67	36.35	$Co^{Oh}_{0.974}Co^{Td}_{0.026}(OH)_{1.974}(SCN)_{0.026}(H_2O)_{0.3}(C_2H_6O)_{0.33}$

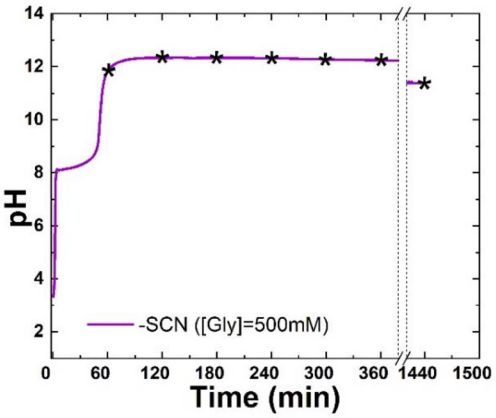

Fig. 5 Precipitation curve of α-Co-SCN: 100 mM NaSCN, 10 mM Co $(Cl)_2$, and 500 mM glycidol. * highlights the exact moment the solution was filtered. This experiment was carried out at room temperature, under magnetic stirring. The measurement starts after pH value stabilization and the addition of glycidol to the mixture.

tetrahedral position. However, no significant difference is observed at the position of the double peak of Co^{Td} in thiocyanate compounds. This suggests that thiocyanate is present in the interlayer space in all seven compounds. ATR-FTIR in Fig. 6c shows the O–H peak at 3400 for α-Co-SCN and 3492 cm^{-1} for α-Co-Cl in all the hydroxides, respectively. The water in the structure is observed at the same position at 1624 cm^{-1} wavenumber exhibiting O–H bending. Fig. 6c exhibits a strong peak at 2060 cm^{-1} in α-Co-SCN-1 h that represents N-bonding. This peak starts to lose its intensity over time while another one at 2180 cm^{-1} representing thiocyanate end-to-end bridging appears and begins to intensify.[49–51] This result shows that we can simply modulate the connection between thiocyanate and the hydroxide layers with the time parameter (Scheme 2). Fig. 6 illustrates that α-Co-SCN-1 h and α-Co-SCN-24 h are the only pure α-Co phase compounds. The XPS survey spectra in Fig. S8.1† successfully confirm the chemical composition of α-Co-SCN-1 h, exhibiting the peaks of Co, C, S, and N. Moreover, a minor peak for Cl is observed, indicating a small amount of chloride present in the sample. Specifically, the estimated SCN to Cl ratio is 19 : 1. Additionally, high-resolution XPS of Co shown in Fig. S8.2† confirms the presence of cobalt in oxidation state II in α-Co-SCN-1 h.[48]

An SEM study was carried out to confirm the morphology of these materials. Fig. S9† shows the SEM images of α-Co-SCN-1 h and α-Co-SCN-24 h, both exhibiting a flower-like morphology. The precipitation time does not alter the morphology of these compounds.

The elemental analysis shown in Table 2 was performed again. α-Co-SCN-1 h is compared to the 24 h compound exposed to the first EA measurement. Interestingly, α-Co-SCN-1 h contains more pseudohalide and tetrahedral cobalt than the 24 h compound. α-Co-SCN-1 h and α-Co-C_4N_3 exhibit a similar percentage of pseudohalide in their α-Co

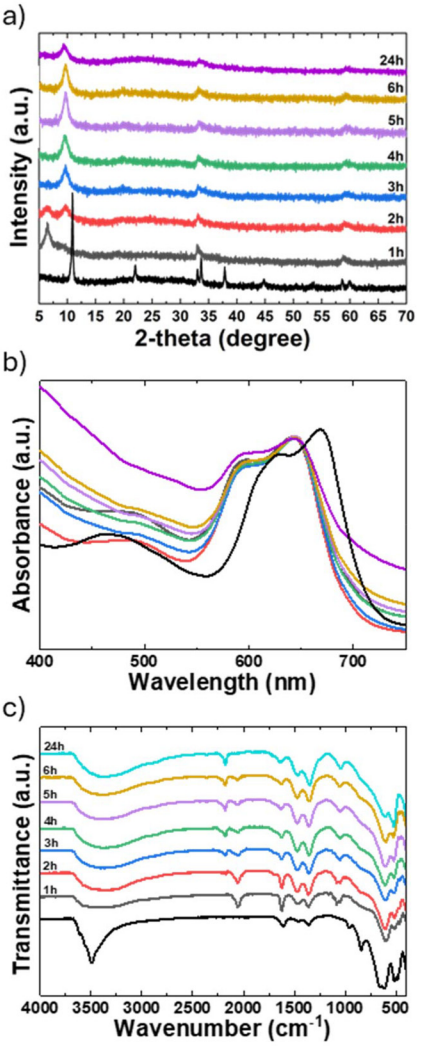

Fig. 6 (a) X-ray powder diffraction, (b) UV-Vis and (c) attenuated total reflectance Fourier-transform infrared spectroscopy (ATR-FTIR) of the different phases of α-Co-SCN. The black spectrum represents α-Co-Cl. This figure shows the evolution of thiocyanate compounds over time.

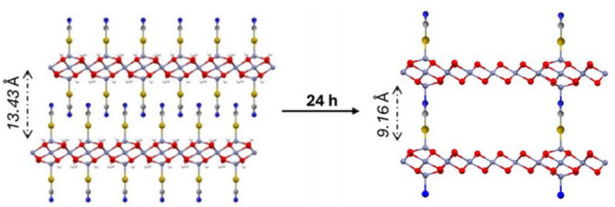

Scheme 2 Representation of α-Co-SCN-1 h (N bonding) and α-Co-SCN-24 h (end-to-end bridging) structural evolution.

structures as indicated by elemental analysis. This finding establishes a basis for a direct comparison between the two compounds, enabling us to evaluate their magnetic properties properly.

Table 2 The estimated formula established by the elemental analysis of α-Co-SCN-1 h, put side by side with α-Co-SCN shown previously in this work

Sample	C%	N%	S%	H%	O%	Phase
α-Co-SCN-1 h	7.14	3.16	7.29	2.14	29.65	$Co^{Oh}_{0.74}Co^{Td}_{0.26}(OH)_{1.74}(SCN)_{0.26}(H_2O)_{0.01}(C_2H_6O)_{0.2}$
α-Co-SCN	7.36	0.35	0.64	2.67	36.35	$Co^{Oh}_{0.974}Co^{Td}_{0.026}(OH)_{1.974}(SCN)_{0.026}(H_2O)_{0.3}(C_2H_6O)_{0.33}$

Magnetism

The magnetic behavior of Co-based hydroxides is diverse. Previous studies have demonstrated the magnetic response of various cobalt-based hydroxide systems with different interlayer anions, including some pseudohalides,[52–55] revealing differences in their composition, structure, and magnetic properties.[6,14–16,56,57]

Fig. 7a illustrates the DC susceptibility (χ_M) as a function of temperature under an applied field of 1000 Oe. The data reveal an increase in susceptibility as the temperature decreases, starting from 50 K and reaching maximum values of 2.87 and 1.07 emu mol^{-1} at 2 K for the samples α-Co-SCN-1 h and α-Co-Cl, respectively. The extracted Curie–Weiss temperatures (θ_{CW}) are 20.3 K, 27.17 K, and 8.03 K for α-Co-Cl, α-Co-SCN-1 h, and α-Co-C_4N_3, respectively, all exhibiting $\theta_{CW} > 0$. These positive values indicate a predominant ferromagnetic behavior in the samples. Previous studies, such as those by Neilson *et al.*, have highlighted the contributions of tetrahedral and octahedral cobalt sites to the magnetic behavior of α-structured materials.[58] This work describes a spin arrangement with in-plane ferromagnetically coupled spins on octahedral cobalt sites that are antiferromagnetically aligned to adjoining tetrahedral sites. This demonstrates that, in our samples, the predominant interaction is driven by the spin within the planes on octahedral cobalt sites, in agreement with our portion of the tetrahedral cobalt.[58]

The blocking temperature (T_B), also called in some papers as the critical temperature (T_c),[58] determined from the field-

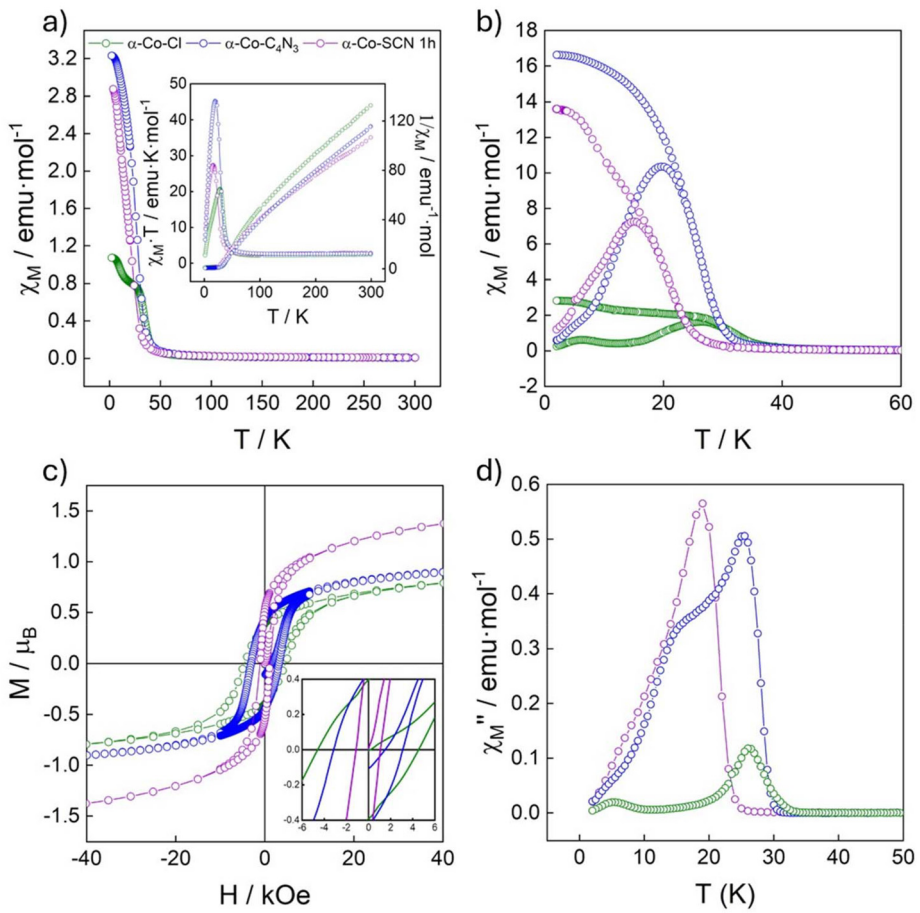

Fig. 7 Magnetic properties of (green) α-Co-Cl, (blue) α-Co-C_4N_3, and (purple) α-Co-SCN-1 h. (a) Outset: magnetic susceptibility as a function of temperature (χ_M *vs.* T)/inset: thermal dependence of $\chi_M \cdot T$ and the fitting of $1/\chi_M$ to the Curie–Weiss law, (b) field-cooled and zero-field-cooled (FC/ZFC), (c) hysteresis loop recorded at 2 K and (d) thermal dependence of dynamic susceptibility for the out-of-phase (χ''_M) signal at 1 Hz.

cooled (FC) and zero-field-cooled (ZFC) measurements shown in Fig. 7b, reveals similarities between the halide and pseudohalide substitutions (Table 3).

Fig. 7c presents the hysteresis loops for α-Co-Cl (green), α-Co-C_4N_3 (blue), and α-Co-SCN (red). The coercive field (H_c) values for each compound, reported in Table 3, indicate that all three materials exhibit hard magnetic properties (H_c > 1000 Oe). Nevertheless, tricyanomethanide and thiocyanate substitution in cobalt-based LH displays a higher coercive field than reported in a related work inserting another pseudohalide, diisocyanoazanide (C_2N_3), in a cobalt-based system.[53]

Although the data in Table 3 show a potential tendency between the coercive field and the basal distance, the dissimilarity in the amount of tetrahedral cobalt does not allow for a clear comparison due to the difference between FM (Co^{Oh}–Co^{Oh} and Co^{Td}–Co^{Td}) and AFM (Co^{Oh}–Co^{Td}) interactions.[8,58]

The magnetization temperature (T_M), corresponding to the onset of spontaneous magnetization, was derived from the AC susceptibility measurements shown in Fig. 7d. The results indicate that T_M is approximately equivalent to T_B for all samples ($T_M \approx T_B$). Among the compounds, α-Co-Cl exhibits the highest ordering temperature, reaching 35 K.

Furthermore, the appearance of double peaks in AC and FC/ZFC characterization has been interpreted as an indication

Table 3 Summary of magnetic parameters

Sample	Co^{Td}	d_B (Å)	xT_{RT} (emu K mol^{-1})	C (emu K mol^{-1})	θ_{CW} (K)	T_M (K)	T_B (K)	H_c (Oe)	M_s (μB)
α-Co-Cl	0.31	8.07	2.26	2.44	20.3	35	31	4580	0.83
α-Co-C_4N_3	0.22	11.46	2.54	2.63	8.03	31	25	3130	0.98
α-Co-SCN-1 h	0.26	13.43	2.81	3.04	27.17	25	19	1100	1.43

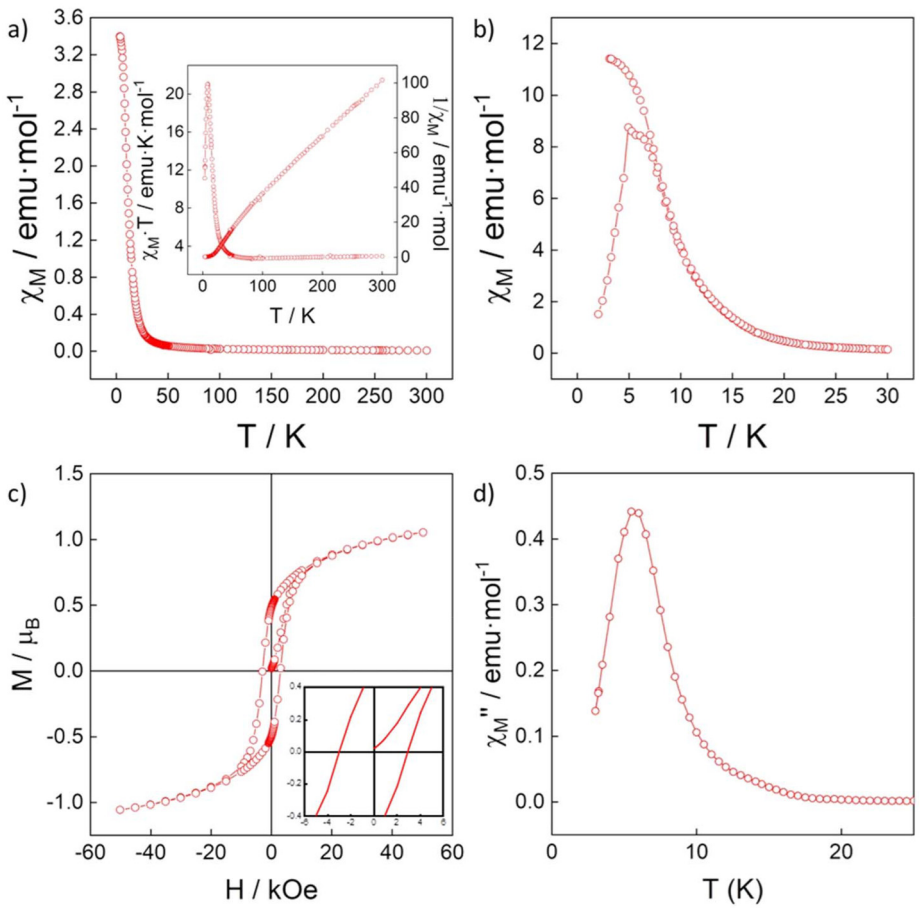

Fig. 8 Magnetic properties of α-Co-SCN-24 h. (a) Outset: magnetic susceptibility as a function of temperature (χ_M *vs.* T)/inset: thermal dependence of $\chi_M \cdot T$ and the fitting of $1/\chi_M$ to the Curie–Weiss law, (b) field-cooled and zero-field-cooled (FC/ZFC), (c) hysteresis loop recorded at 2 K and (d) thermal dependence of dynamic susceptibility for the out-of-phase (χ''_M) signal at 1 Hz.

of the existence of distinct sublattices or microdomains within the structure.[6,58]

Previous studies suggested that the interlayer distance may play a role in the magnetic response of the α structure.[18] Specifically, research has demonstrated a distinction between the magnetic behavior of structures intercalated with odd and even numbers of dicarboxylic acid molecules within the interlayer space. The magnetic response varies with the interlayer space ranging from approximately 10–11 Å for n = 1 to 12–13 Å for n = 2, with $T_M(n = 1) < T_M(n = 2)$. In this study, the same tendency is observed. Specifically, the pseudohalide substituent α-Co-SCN-1 h and α-Co-C_4N_3 exhibit a basal distance comparable to those of n = 2 and n = 1, respectively. These alterations in the magnetic properties of these compounds have been shown to be likely linked to variations in the alignment and/or twisting of the organic molecules, inducing subtle structural modifications that influence the interaction between the two sublattices (Oh and Td).[18]

As expected, the magnetic properties of α-Co-SCN-24 h exhibit a behavior analogous to the β structure with magnetic ordering occurring at lower temperatures (Fig. 8).[59] The system shows ferromagnetic dominance with a positive Curie–Weiss temperature (θ_{CW} = 14.2 K). The blocking temperature and the magnetization temperature extracted from DC (FC/ZFC) and AC measurements, respectively, are recorded at 11 K and 12 K. The hysteresis loop shows a coercive field at 3016 Oe, higher than 1000 Oe, like α-Co-SCN-1 h. The coordination of thiocyanate did not alter the hard magnetic behavior. However, α-Co-SCN-24 h records the smallest amount of tetrahedral cobalt in its structure (Table 1); as a result, we have a higher amount of Co^{Oh}–Co^{Oh} interactions and fewer Co^{Oh}–Co^{Td} ones.[6] This explains the similarity between α-Co-SCN-24 h and cobalt-based layered hydroxide without a tetrahedral environment (*i.e.* β-phase and LDH).[15,59]

Overall, these results demonstrate that the chemical and structural versatility of *Simonkolleite*-like simple hydroxides serves as a magnetic playground to explore the design of new magnetic hybrid materials with dynamic structures.

Conclusions

Pseudohalide substitution with SCN^- and $C_4N_3^-$ has been successfully achieved in α-cobalt-layered hydroxides by optimizing the epoxide route, providing detailed insights into their structural and magnetic properties. While tricyanomethanide ($C_4N_3^-$) substitution had been previously explored, this work offers a more comprehensive analysis, particularly highlighting the distinctive behavior of thiocyanate (SCN^-). The incorporation of SCN^- induces subtle yet important structural changes, including a time-dependent evolution leading to the formation of interlayer bridges within 24 hours of precipitation. The introduction of pseudohalides into α-Co-SCN-1 h and α-Co-C_4N_3, alongside halide substitutions, results in a hard magnetic behavior characterized by a coercive field exceeding 1000 Oe. The magnetic response of α-Co-SCN-24 h aligns with the existing literature, where a lower amount of tetrahedral cobalt leads to a magnetic behavior resembling that of layered double hydroxide (LDH) structures. This similarity suggests that the dominant interactions in α-Co-SCN-24 h arise from Co^{Oh}–Co^{Oh} coupling, as the reduction in tetrahedral cobalt decreases Co^{Oh}–Co^{Td} interactions. These findings reinforce the link between structure and magnetism, highlighting the role of octahedral/tetrahedral cobalt coordination in cobalt-based layered hydroxides. Indeed, while pseudohalide substitution influences magnetic behavior, its impact is minor compared to the more significant structural changes induced by substitutions. This study provides new insights into the role of pseudohalide substitutions and confirms the presence of interlayer bridges, addressing a critical gap in the understanding of α-cobalt-based layered hydroxides. By clarifying how pseudohalide and halide substitutions influence both structure and magnetism, it paves the way for tailoring these materials for specific applications.

Author contributions

Youssra Diouane: investigation, conceptualization, formal analysis, original draft writing. Alvaro Seijas-Da Silva: conceptualization, formal analysis, review and editing. Víctor Oestreicher: investigation, conceptualization. Gonzalo Abellán: conceptualization, resources, management, validation, review and editing, supervision.

Data availability

The data supporting this article have been included as part of the ESI.†

Conflicts of interest

There are no conflicts to declare.

Acknowledgements

The project SEAL HYDROGEN is supported by the Clean Hydrogen Partnership and its members under GA 101137915. This work was supported by the European Research Council (ERC Starting Grant No. 2D-PnictoChem 804110, and ERC Proof of Concept Grant 2D4H2 No. 101101079), the Spanish MCIN/AEI/10.13039/501100011033 (PID2022-143297NB–I00, TED2021-131347B–I00 and Unit of Excellence "Maria de Maeztu" CEX2019-000919-M), and the Generalitat Valenciana (CIDEGENT/2018/001). Y. D. thanks the Generalitat Valenciana for a Santiago Grisolía predoctoral fellowship (GRISOLIAP/2021/001). A. S.-D thanks the Universidad de Valencia for an 'Atracció de talent' predoctoral grant. VO is a member of ALN. The authors thank Christian Olivares-Martínez and Federico

Juarez for their assistance with the experimental work, and Diego Hunt for the fruitful discussions.

References

1 K.-H. Goh, T.-T. Lim and Z. Dong, *Water Res.*, 2008, **42**, 1343–1368.
2 C. Taviot-Guého, V. Prévot, C. Forano, G. Renaudin, C. Mousty and F. Leroux, *Adv. Funct. Mater.*, 2018, **28**, 1703868.
3 C. Jaramillo-Hernández, A. Seijas-Da Silva and G. Abellán, *Eur. J. Inorg. Chem.*, 2025, **28**, e202400754.
4 G. W. Brindley and C.-C. Kao, *Phys. Chem. Miner.*, 1984, **10**, 187–191.
5 Y. Du and D. O'Hare, *Inorg. Chem.*, 2008, **47**, 3234–3242.
6 V. Oestreicher, C. Dolle, D. Hunt, M. Fickert and G. Abellán, *Nano Mater. Sci.*, 2022, **4**, 36–43.
7 M. Shao, R. Zhang, Z. Li, M. Wei, D. G. Evans and X. Duan, *Chem. Commun.*, 2015, **51**, 15880–15893.
8 V. Oestreicher, D. Hunt, R. Torres-Cavanillas, G. Abellán, D. A. Scherlis and M. Jobbágy, *Inorg. Chem.*, 2019, **58**, 9414–9424.
9 J. A. Carrasco, R. Sanchis-Gual, A. S.-D. Silva, G. Abellán and E. Coronado, *Chem. Mater.*, 2019, **31**, 6798–6807.
10 J. Romero, H. Prima-Garcia, M. Varela, S. G. Miralles, V. Oestreicher, G. Abellán and E. Coronado, *Adv. Mater.*, 2019, **31**, 1900189.
11 Y. Wang, D. Yan, S. El Hankari, Y. Zou and S. Wang, *Adv. Sci.*, 2018, **5**, 1800064.
12 M. P. Browne, Z. Sofer and M. Pumera, *Energy Environ. Sci.*, 2019, **12**, 41–58.
13 A. Seijas-Da Silva, R. Sanchis-Gual, J. A. Carrasco, V. Oestreicher, G. Abellán and E. Coronado, *Batteries Supercaps*, 2020, **3**, 499–509.
14 P. Rabu, E. Delahaye and G. Rogez, *Nanotechnol. Rev.*, 2015, **4**, 557–580.
15 J. A. Carrasco, S. Cardona-Serra, J. M. Clemente-Juan, A. Gaita-Ariño, G. Abellán and E. Coronado, *Inorg. Chem.*, 2018, **57**, 2013–2022.
16 J. A. Carrasco, V. Oestreicher, A. S.-D. Silva and G. Abellán, *Appl. Clay Sci.*, 2023, **243**, 107073.
17 G. Abellán, E. Coronado, C. Martí-Gastaldo, J. Waerenborgh and A. Ribera, *Inorg. Chem.*, 2013, **52**, 10147–10157.
18 V. Oestreicher, D. Hunt, C. Dolle, P. Borovik, M. Jobbágy, G. Abellán and E. Coronado, *Chem. – Eur. J.*, 2021, **27**, 921–927.
19 M. Kurmoo, *Mol. Cryst. Liq. Cryst. Sci. Technol., Sect. A*, 2000, **342**, 167–176.
20 H. Ji, J. Cai, N. Gan, Z. Wang, L. Wu, G. Li and T. Yi, *Chem. Cent. J.*, 2018, **12**, 136.
21 Z. Qin, *Symmetry*, 2023, **15**, 1329.
22 A. J. Lewis, E. Nakamaru-Ogiso, J. M. Kikkawa, P. J. Carroll and E. J. Schelter, *Chem. Commun.*, 2012, **48**, 4977.
23 Z. Xu, M. Chen and S. (Frank) Liu, *J. Energy Chem.*, 2019, **36**, 106–113.
24 L. Váhovská, S. Vitushkina, I. Potočňák, Z. Trávníček and R. Herchel, *Dalton Trans.*, 2018, **47**, 1498–1512.
25 C. Carteret, B. Grégoire and C. Ruby, *Solid State Sci.*, 2011, **13**, 146–150.
26 V. Chandrasekhar, A. Dey, A. J. Mota and E. Colacio, *Inorg. Chem.*, 2013, **52**, 4554–4561.
27 A. Seijas-Da Silva, V. Oestreicher, C. Huck–Iriart, M. Mizrahi, D. Hunt, V. Ferrari and G. Abellán, *Batteries Supercaps*, 2024, e202400335.
28 V. Oestreicher and M. Jobbágy, *Langmuir*, 2013, **29**, 12104–12109.
29 J. Vallejo, M. Viciano-Chumillas, F. Lloret, M. Julve, I. Castro, J. Krzystek, M. Ozerov, D. Armentano, G. De Munno and J. Cano, *Inorg. Chem.*, 2019, **58**, 15726–15740.
30 Y. Du, K. M. Ok and D. O'Hare, *J. Mater. Chem.*, 2008, **18**, 4450.
31 J. A. Carrasco, G. Abellán and E. Coronado, *J. Mater. Chem. C*, 2018, **6**, 1187–1198.
32 Y. Li, Y. Zou and Y. Hou, *Cryst. Res. Technol.*, 2011, **46**, 305–308.
33 S. A. Hassanzadeh-Tabrizi, *J. Alloys Compd.*, 2023, **968**, 171914.
34 M. Halma, K. Aparecidadiasdefreitascastro, C. Taviotgueho, V. Prevot, C. Forano, F. Wypych and S. Nakagaki, *J. Catal.*, 2008, **257**, 233–243.
35 G. Abellán, J. A. Carrasco and E. Coronado, *Inorg. Chem.*, 2013, **52**, 7828–7830.
36 V. Oestreicher and M. Jobbágy, *Chem. – Eur. J.*, 2019, **25**, 12611–12619.
37 R. Ma, Z. Liu, K. Takada, K. Fukuda, Y. Ebina, Y. Bando and T. Sasaki, *Inorg. Chem.*, 2006, **45**, 3964–3969.
38 X. Xia, J. Liu, Y. Liu, Z. Lei, Y. Han, Z. Zheng and J. Yin, *Coatings*, 2023, **13**, 224.
39 P. Nie, L. Shen, H. Luo, H. Li, G. Xu and X. Zhang, *Nanoscale*, 2013, **5**, 11087.
40 J. Palion-Gazda, B. Machura, F. Lloret and M. Julve, *Cryst. Growth Des.*, 2015, **15**, 2380–2388.
41 J. S. Haynes, A. Kostikas, J. R. Sams, A. Simopoulos and R. C. Thompson, *Inorg. Chem.*, 1987, **26**, 2630–2637.
42 P. Bhowmik, S. Chattopadhyay, M. G. B. Drew, C. Diaz and A. Ghosh, *Polyhedron*, 2010, **29**, 2637–2642.
43 A. Seijas-Da Silva, V. Oestreicher, E. Coronado and G. Abellán, *Dalton Trans.*, 2022, **51**, 4675–4684.
44 J. A. Carrasco, A. Seijas-Da Silva, V. Oestreicher, J. Romero, B. G. Márkus, F. Simon, B. J. C. Vieira, J. C. Waerenborgh, G. Abellán and E. Coronado, *Chem. – Eur. J.*, 2020, **26**, 6504–6517.
45 V. Oestreicher, G. Abellán and E. Coronado, *Phys. Status Solidi RRL*, 2020, **14**, 2000380.
46 E. Boccalon, G. Gorrasi and M. Nocchetti, *Adv. Colloid Interface Sci.*, 2020, **285**, 102284.
47 T. Shinagawa, N. Kotobuki and A. Ohtaka, *Nanoscale Adv.*, 2023, **5**, 96–105.
48 M. C. Biesinger, B. P. Payne, A. P. Grosvenor, L. W. M. Lau, A. R. Gerson and R. St C. Smart, *Appl. Surf. Sci.*, 2011, **257**, 2717–2730.

49 R. A. Bailey, S. L. Kozak, T. W. Michelsen and W. N. Mills, *Coord. Chem. Rev.*, 1971, **6**, 407–445.
50 S. Satapathi, S. Das, K. Bhar, R. K. Kumar, T. K. Maji and B. K. Ghosh, *Polyhedron*, 2011, **30**, 387–396.
51 H.-L. Jia, M.-J. Jia, G.-H. Li, Y.-N. Wang, J.-H. Yu and J.-Q. Xu, *Dalton Trans.*, 2013, **42**, 6429.
52 A. Beghidja, S. Hallynck, R. Welter and P. Rabu, *Eur. J. Inorg. Chem.*, 2005, **2005**, 662–669.
53 J. L. Manson, C. R. Kmety, Q. Huang, J. W. Lynn, G. M. Bendele, S. Pagola, P. W. Stephens, L. M. Liable-Sands, A. L. Rheingold, A. J. Epstein and J. S. Miller, *Chem. Mater.*, 1998, **10**, 2552–2560.
54 M. Kurmoo and C. J. Kepert, *New J. Chem.*, 1998, **22**, 1515–1524.
55 S. R. Marshall, C. D. Incarvito, J. L. Manson, A. L. Rheingold and J. S. Miller, *Inorg. Chem.*, 2000, **39**, 1969–1973.
56 G. Abellán, C. Martí-Gastaldo, A. Ribera and E. Coronado, *Acc. Chem. Res.*, 2015, **48**, 1601–1611.
57 M. Kurmoo, *Chem. Mater.*, 1999, **11**, 3370–3378.
58 J. R. Neilson, D. E. Morse, B. C. Melot, D. P. Shoemaker, J. A. Kurzman and R. Seshadri, *Phys. Rev. B:Condens. Matter Mater. Phys.*, 2011, **83**, 094418.
59 Z. Wang and M. S. Seehra, *J. Phys.: Condens. Matter*, 2017, **29**, 225803.